International Journal of Hydrogen Energy 262 (2026) 156827

Contents lists available at ScienceDirect

International Journal of Hydrogen Energy

journal homepage: www.elsevier.com/locate/he

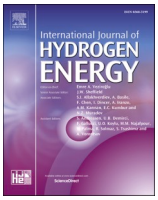

Insights into depth-dependent degradation of Pt/C fuel cell catalysts from *operando* X-ray scattering

Stefanie Punke [a], Jannik Heitz [b,c], Rebecca K. Pittkowski [a], Jens Edelvang-Pejrup [a], Aline Bornet [d], Jakub Drnec [e], Jacob J.K. Kirkensgaard [f,g], Thomas Kadyk [b], Kirsten M.Ø. Jensen [a,*], Matthias Arenz [d,**]

[a] Department of Chemistry and Nano-Science Center, University of Copenhagen, Copenhagen, 2100, Denmark
[b] Theory and Computation of Energy Materials (IET-3), Institute of Energy Technologies, Forschungszentrum Jülich GmbH, Jülich, 52428, Germany
[c] Chair of Theory and Computation of Energy Materials, Faculty of Georesources and Materials Engineering, RWTH Aachen University, Aachen, 52062, Germany
[d] Department of Chemistry, Biochemistry and Pharmaceutical Sciences, University of Bern, Bern, 3012, Switzerland
[e] ESRF - The European Synchrotron, Grenoble, 38000, France
[f] Niels Bohr Institute, University of Copenhagen, Denmark, Copenhagen, 2100, Denmark
[g] Department of Food Science, University of Copenhagen, Frederiksberg, 1958, Denmark

ARTICLE INFO

Keywords:
Operando
X-ray scattering
ORR
Degradation mechanisms
Modelling

ABSTRACT

Long-term durability remains a critical challenge for Proton Exchange Membrane Fuel Cells (PEMFCs). While degradation mechanisms have been identified, their quantitative contributions to performance loss have not been conclusively determined. Here, we systematically investigate the degradation of two Pt/C PEMFC catalysts with distinct average particle sizes using a newly developed operando cell that combines X-ray total scattering with Pair Distribution Function analysis, X-ray Diffraction, and Small-Angle X-ray Scattering (SAXS). By combining these techniques, particularly through a sophisticated Monte Carlo analysis of the SAXS data, depth- and time-resolved particle size distributions are obtained, enabling direct tracking of particle size evolution throughout the catalyst layer. Coupled with a physico-statistical model, this approach enables the identification and quantitative separation of system-specific degradation pathways, including particle agglomeration, coalescence, and Ostwald ripening. The results reveal pronounced depth-dependent degradation, strongest near the catalyst/microporous transport layer interface, and identify Ostwald ripening as the dominant degradation mechanism.

1. Introduction

Global warming demands urgent reductions in greenhouse gas emissions, making the development of sustainable energy technologies imperative [1]. A promising alternative to traditional combustion engines is the Proton Exchange Membrane Fuel Cell (PEMFC), particularly for heavy-duty vehicles [2,3]. Current state-of-the-art PEMFC catalysts predominantly use precious metals like Pt or Pt-based alloyed nanoparticles [4]; however, their long-term activity and durability are limited due to various degradation processes [5–14]. These degradation mechanisms within the catalyst layer include (i) particle agglomeration and coalescence, (ii) electrochemical Ostwald ripening, (iii) metal dissolution, and (iv) particle detachment from the support [5,15–17]. Collectively, these processes give rise to complex, coupled degradation behavior within the already heterogeneous catalyst layer environment. Consequently, disentangling the individual contributions of each mechanism remains challenging, and a comprehensive understanding of catalyst degradation is still lacking.

To advance catalyst degradation studies, Accelerated Stress Tests (ASTs) are commonly employed to mimic long-term operational effects within experimentally accessible timescales. These tests typically involve load-cycle or start–stop protocols, such as those recommended by the Fuel Cell Commercialization Conference of Japan (FCCJ) [18]. Load cycles simulate operating conditions of the fuel cell, in the FCCJ protocol consisting of alternating potential holds of 3 s between 0.6 and 1.0 V versus the reversible hydrogen electrode (V_{RHE}), whereas start–-stop conditions involve potential sweeps from 1.0 to 1.5 V_{RHE}. Combining both protocols provides more realistic and comprehensive

* Corresponding author.
** Corresponding author.
E-mail addresses: kirsten@chem.ku.dk (K.M.Ø. Jensen), matthias.arenz@unibe.ch (M. Arenz).

https://doi.org/10.1016/j.ijhydene.2026.156827
Received 19 June 2026; Received in revised form 25 July 2026; Accepted 27 July 2026

stress conditions, enabling improved insight into catalyst degradation [19–21]. However, our understanding of the underlying processes is often limited by the characterization techniques used to probe the catalyst layer under operating conditions. Identical-location scanning and transmission electron microscopy, combined with ASTs, remain among the most widely used approaches. These methods provide highly detailed local information by examining the same region before and after degradation; however, they inherently suffer from limited statistical representativeness [15,20,22–29]. An alternative approach, *ex situ* small-angle X-ray scattering (SAXS) of samples subjected to ASTs in a gas diffusion electrode (GDE) setup, offers improved statistical sampling over larger sample volumes [20,30,31]. Nonetheless, its *ex situ* nature restricts observations to the beginning and end states, hindering the direct tracking and modelling of degradation pathways. Therefore, *operando* investigations of the catalyst layer during active degradation are essential for developing more durable and optimized fuel cell systems.

Recent advances in synchrotron radiation have enabled such studies through *operando* and *in situ* X-ray techniques, allowing catalyst characterization under realistic operating conditions [5,10,11,16,32–35]. These approaches have gained significant traction, particularly the combination of different X-ray techniques. One example is SAXS and X-ray absorption spectroscopy (XAS), which enables simultaneous determination of particle size from SAXS and information on the Pt oxidation state and local atomic environment from XAS [36,37]. Another powerful combination is SAXS and X-ray diffraction (XRD), which allows changes in particle size and crystallite size to be distinguished. This combination has recently been employed to probe spatial heterogeneity in catalyst degradation across the gas diffusion layer (GDL), as demonstrated using micro-focused XRD and SAXS by Schröder et al. [10] However, these studies did not resolve depth-dependent degradation in GDE configurations with oxygen supplied from the GDL side. To address this limitation, we employ *operando* X-ray scattering measurements in a GDE operated in self-breathing mode, combining the experimental control of a three-electrode aqueous setup with mass transport conditions closer to practical devices [38,39]. In addition, we integrate a physico-statistical modelling framework to quantitatively analyze the underlying degradation mechanisms.

By employing quasi-simultaneous operando total scattering (TS) with Pair Distribution Function (PDF) analysis, XRD, and SAXS, we monitor catalyst degradation across multiple length scales and electrode layer depths, spanning Ångström to nanometer regimes [40,41]. XRD provides insight into crystal structure and crystallite size evolution, while PDF analysis, obtained via Fourier transformation of TS data [42], captures both local and crystal structure information. SAXS enables a comprehensive assessment of particle morphology and size distributions. Importantly, a Monte Carlo-based analysis of the SAXS data allows extraction of particle radius distributions (PRDs) without assuming a predefined functional form, thereby minimizing model bias. The use of a micro-focused X-ray beam (~5 μm) at the ID31 beamline at the European Synchrotron Radiation Facility (ESRF) enables depth-resolved measurements with high spatial precision, facilitating detailed analysis of degradation as a function of electrode depth [43,44].

To complement the experimental observations, the evolution of the PRDs is analyzed using a physico-statistical model of catalyst degradation that incorporates dissolution and redeposition (Ostwald ripening), coagulation (encompassing agglomeration and coalescence), and particle detachment [45]. The model is fitted to the experimental PRDs using Bayesian inference, enabling quantitative mechanistic deconvolution while rigorously accounting for uncertainty. In this framework, modelling serves as a complementary interpretative tool to identify which degradation pathways are most consistent with the observed structural evolution. This integrated methodology is applied to commercial Pt/C catalysts with small (~12 Å radius) and large (~26 Å radius) nanoparticles under identical operating conditions.

Our combined experimental and modelling approach provides unprecedented, depth-resolved insight into PEMFC catalyst degradation. The results demonstrate that the commonly assumed lognormal particle size distribution does not adequately describe systems undergoing ripening and agglomeration, thereby complicating mechanistic interpretation [17]. Furthermore, comparison of catalysts with different initial particle sizes reveals pronounced size-dependent degradation behavior. Importantly, studies conducted in aqueous or non-breathing environments may significantly underestimate degradation severity, as highlighted by the pronounced spatial heterogeneity observed within the catalyst layer. These findings underscore the critical importance of depth-resolved catalyst layer design for improving PEMFC durability and performance.

2. Methods

The catalyst ink and Working Electrode (WE) were prepared following the method previously described by Schröder et al. [10] The preparation procedure is briefly reiterated here, as well as described in greater detail in the SI, section 1. The *operando* measurements were conducted at the ID31 beamline at the ESRF.

2.1. Ink preparation

We used ultrapure Milli-Q water (resistivity >18.2 MΩ· cm and total organic carbon <5 ppb) from a Millipore system for the catalyst ink preparation. To prepare the catalyst ink, isopropanol (IPA, 99.7+ %, Alfa Aesar), commercial Pt catalysts supported on Carbon (Pt/C) [TEC10E20A (1−2 nm Pt/C and 19.4 wt % Pt) and TEC10E50E-HT (4−5 nm Pt/C and 50.6 wt % Pt), Tanaka kikinzoku kogyo], and Nafion dispersion (D1021, 10 wt %, EW 1100, Fuel Cell Store) were used. We will refer to the different sized Pt catalysts as 'small' and 'large' systems from now on. The WE was made of a GDL with a microporous layer (MPL) on top (Freudenberg H23C8, 230 μm thick). The *operando* cell was cleaned via boiling in Milli-Q water for 15 min.

As for the preparation of the catalyst ink, the catalysts were dispersed in a mixture of Milli-Q water and IPA (water/IPA volume ratio of 3:1) with a Pt concentration of 0.05 mg/mL. The dispersions were sonicated for 5 min in a sonication bath (Bioblock Scientific, T 310/H, 35 kHz). Before the vacuum filtration, we added the appropriate amount of the ionomer Nafion (Nafion/carbon mass ratio of 1:1) and sonicated the dispersion again for 5 min in the sonication bath.

2.2. Working electrode - vacuum filtration

In a vacuum filtration setup, the Freudenberg GDL + MPL was placed between a glass funnel and a sand core filter. Following the method described by Yarlagadda et al., [46] this assembly was positioned on a collecting bottle. After sonicating the mixture for 1 min in a sonication bath, the diluted ink was poured into the funnel. The catalyst was then deposited onto the GDL + MPL using a diaphragm vacuum pump (Vacuubrand, MZ 2C, with a maximum flow rate of 1.7 m^3/h and a pressure of 9.0 mbar). The GDL + MPL was allowed to dry and was stored in air. This process resulted in a nominal platinum loading of 0.200 mg/cm^2. For electrochemical measurements, the GDL + MPL was cut into narrow slices measuring 12 × 3 mm^2 after vacuum filtration.

2.3. Electrochemical cell and measurements

An *operando* cell (Fig. S1) described in more detail by Wiberg et al. [38] was used with Ar-saturated (BIP ultrahigh purity, Air Liquide) 0.1 M H_2SO_4 as electrolyte (99% H_2SO_4, Suprapure, Sigma-Aldrich). The electrolyte was degassed before being introduced from the side, just above the catalyst layer, then circulated through the cell, and eventually discarded. Our vacuum-filtrated catalyst layer was used as the WE, a Pt wire as the Counter Electrode (CE), and an Ag/AgCl electrode (Leakless Miniature Ag/AgCl Reference Electrode, eDAQ) was used as Reference

Electrode (RE). The shift of the Ag/AgCl reference electrode compared to an RHE was determined before and after each measurement. An overview of the shift can be found in Table S1. All potentials are reported versus reversible hydrogen electrode (V_{RHE}) in the following. The electrochemical measurements were conducted using a BioLogic SP-240 potentiostat. The conditioning CVs and potential holds recorded before and after the AST were compensated for 80% of the solution resistance, while the AST itself was not. The solution resistance was approximately 18 Ω.

The catalyst was conditioned with 20 CVs between 0.05 and 1.1 V_{RHE} using a scan rate of 50 mV/s in air. Afterwards, we applied potential holds of 0.4 and 0.9 V_{RHE} for 25 min to record the X-ray scattering at the catalyst's Beginning of Life (BoL). The first cycle of the AST consisted of 50 times applying potential steps between 0.6 and 1.0 V_{RHE} (3 s holding per potential). We have then added two CVs from 1.0 to 1.5 V_{RHE} with a scan rate of 100 mV/s. These combinations of 50 potential steps with two CVs were repeated until a total of 2000 load cycles were reached. To probe the End of Life (EoL) of our catalyst, we again applied a potential of 0.4 V_{RHE} before another round of conditioning in the form of 5 CVs as previously described. We concluded the measurement with another final potential hold of 0.4 V_{RHE}. A more detailed overview of the protocol can be found in Table S2 and Fig. S2, as well as a comparison between the current densities of the first 50 load cycles to the last for the small and large systems, respectively, see Figs. S3 and S4.

2.4. Operando measurements

The SAXS, WAXS, and TS data were collected with a 75.0 keV X-ray beam. The beam was focused to a vertical size of about 5 µm. A Pilatus 3X CdTe 2 M hybrid photon-counting area detector was positioned at different distances from the electrochemical cell to account for the range from SAXS to TS. To calibrate the detector sample distance for SAXS, we used an AgBh standard and a CeO_2 standard for the XRD and TS detector positions. The detector distances for the SAXS position, XRD position, and TS were 6429 mm, 788 mm, and 342 mm, respectively. The measurements were done quasi-simultaneously, i.e., the detector distance was changed during the measurement sequence.

For each system, we performed a depth profile with one measurement per µm, see Fig. S5. From these scans through the catalyst layer, we identified the scan with the highest Pt scattering intensity and defined it as the 'center' layer, see Fig. 1, which provides a visual overview of the measurement protocol. We also defined the 'bottom' layer as 5 µm below the center layer and the 'top' layer as 5 µm above the center layer. With this setup, there should be no overlap between the bottom, center, and top layers.

We first measured data from the as-prepared catalyst in the cell, i.e., before the impact of any electrochemistry. At this stage (Fig. 1a), we collected XRD, SAXS, and TS data in 10 scans (steps of 1 µm) from the top to the bottom layer. After conditioning, i.e., at the catalyst BoL (Fig. 1b), we collected XRD, SAXS, and TS data from the center layer. During the AST (Fig. 1c), we collected XRD and SAXS data for the bottom, center, and top layers. Finally, at the End of Life (EoL) of the catalyst (Fig. 1d), we collected TS, XRD, and SAXS data in the 10 depth steps.

The collection times for XRD and SAXS were 1 s each and for TS 4 s. The collected 2D images were masked for dead pixels and detector gaps. Afterwards, the data were integrated with pyFAI and normalised by the intensity of the incoming X-ray beam to account for intensity fluctuations [47].

2.5. XRD analysis

The XRD data were corrected by subtracting the background signal, i.e., the cell, the electrolyte, and the carbon support (Ketjenblack EC-300J), see Fig. S6. The instrumental parameters were determined using the diffraction pattern from a CeO_2 standard. Rietveld refinements were performed with TOPAS 7 [48]. We refined a model of metallic Pt with a face-centered cubic (*fcc*) structure (ICSD 243678) to fit the data [49]. For the small nanoparticles, the refinement included the scale factor, lattice parameter, and crystallite size. To account for the background, we refined a Chebychev polynomial of 9 terms. For the data from the larger nanoparticles, we included a fixed microstrain as defined by TOPAS of 0.0018 in the refinement, in addition to the refinement parameters used for the small nanoparticle sample. Exemplary fits for the three layers at BoL and EoL are found in Fig. S7–S10, as well as Table S3–S6.

2.6. Total scattering and PDF analysis

The background correction for the TS measurements was performed the same way as for the XRD measurements, see Fig. S11 for comparison. The PDFs were obtained with PDFgetX3 in xpdfsuite using a r_{poly} of 0.9 Å, a q_{min} of 2 $Å^{-1}$, and a q_{max} of 19.5 $Å^{-1}$ for the sample with larger nanoparticles and a q_{max} of 16.4 and 19.5 $Å^{-1}$ for the sample with smaller nanoparticles at BoL and EoL, respectively [50]. Refinements were conducted with DiffPy-CMI with a Pt *fcc* model (ICSD 243678) and

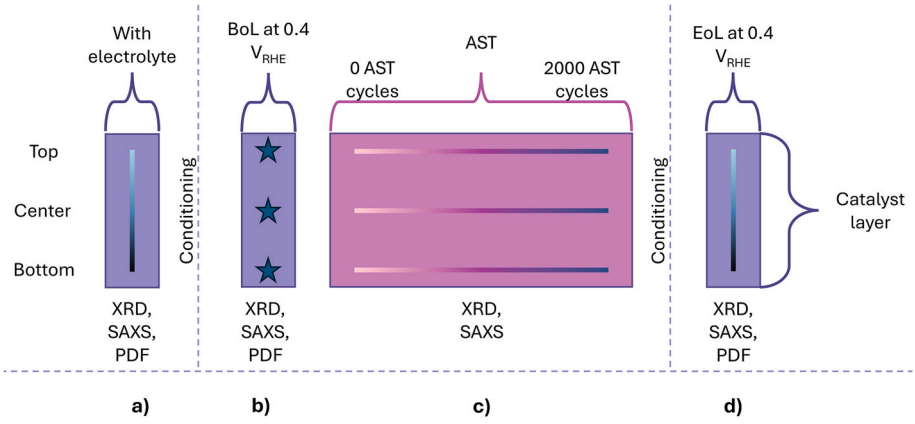

Fig. 1. The purple blocks in a), b) and d) represent stages of the EC protocol when data for all three techniques (XRD, SAXS and PDF) were measured. The colorbar in these blocks corresponds to a depth scan through the catalyst layer, where light blue represents the 'top' (closer to the electrolyte) and black represents the 'bottom' (closer to the GDL; see Fig. S4 for more detail). The blue star symbolizes one measurement at the top, center, and bottom layer. These single measurements were conducted at the AST BoL at 0.4 V_{RHE} and EoL at 0.4 V_{RHE}. The pink block c) represents the AST, where only XRD and SAXS data were measured. The colorbars indicate the AST evolution of the three depths (top, center, bottom), from the start after conditioning at 0.9 V_{RHE} (light pink), i.e., 0 AST cycles, to after 2000 AST cycles at open-circuit potential (dark blue). (For interpretation of the references to color in this figure legend, the reader is referred to the Web version of this article.)

an underlying lognormal distribution of spherical crystalline domains, similar to Gamez-Mendoza et al. [49,51,52] For the small samples, we refined the lattice parameter, the average crystalline domain, and the scale. The standard deviation of the lognormal distribution was set to a fixed value of 3.5 Å and 9 Å for BoL and EoL, respectively, as the refinements otherwise yielded nonphysical results due to a very high correlation of the standard deviation and the average of the lognormal distribution. Further, δ_2 and B_{iso} were fixed to 3.5 Å and 0.6 Å^2, respectively. The refinements of the larger system included the lattice parameter, the average crystalline domain, the scale, δ_2, and B_{iso}. They were also conducted with a fixed standard deviation for the lognormal distribution, here set to 9 Å. Exemplary fits for the three layers are found in Figs. S12–S15, as well as Table S7–S10.

2.7. SAXS analysis

The data were corrected for background scattering of the cell and the support, Ketjen Black, see Fig. S16. The Monte Carlo Analysis was done with McSAS [53]. The analysis was performed over a q-range of 0.03 to 0.4 Å^{-1} for the smaller system, 0.03 to 0.25 Å^{-1} for the large system for the depth scans throughout the AST and 0.03 to 0.4 Å^{-1} for the quantitative analysis. The different limits for the large system are because the higher q limit yielded unphysical results at the lowest catalyst layer. Hence, we have kept the lower limit for a comparison throughout the depths but the higher q limit for a better resolution of the polydispersity of the Monte Carlo analysis. The respective data were rebinned to 100 data points per measurement. The measurement uncertainties were assumed to follow Poisson statistics. We have chosen a spherical model with 300 as the maximal number of contributions to the size distribution over a range of 6 to 70 Å and 13 to 70 Å for the small and the large sample, respectively. The lower limits were set to avoid artefacts in the Monte Carlo analysis. These arise from an intrinsic limitation of SAXS analysis, namely the scattering intensity scales with the square of the particle volume. As a result, extremely small particles contribute only weakly to the overall scattering signal, which can lead to the non-physical results artefacts in the Monte Carlo optimization for these [54]. The maximum number of iterations was set to 100000, and the number of repetitions was set to 50 for both the AST measurement and depth scans. The convergence criterion χ^2 was set to 10 for the smaller system and 20 for the larger system. Exemplary fits for the three layers are found in Fig. S17–S20, as well as Table S11–S14.

2.8. Model-based analysis

To support the experimental analysis, a physical-statistical model of catalyst structural degradation [45,55,56] is fitted to the PRDs obtained from the analysis of the SAXS data. This allows for the deconvolution of dissolution and redeposition (Ostwald ripening), coagulation (particle agglomeration), and particle detachment. In this model, the catalyst is represented as randomly dispersed solid spherical platinum nanoparticles on the carbon support. The model is spatially invariant, so gradients along the electrode thickness or locally within the carbon pores are not resolved.

The evolution of the PRD, $f_N(r,t)$, is described with the continuity equation [45]

$$\frac{\partial f_N(r,t)}{\partial t} = \underbrace{-\frac{\partial}{\partial r}\left[f_N(r,t)\frac{dr}{dt}\right]}_{\text{dissolution/redeposition}} \underbrace{+J^+ - J^-}_{\text{coagulation}} \underbrace{-k_{\text{det}} f_N(r,t)}_{\text{detachment}}. \tag{1}$$

For dissolution and redeposition, growth rate of a particle is given by [56].

$$\frac{dr}{dt} = V_m k_{rdp} \overline{c_{Pt}}(t) \exp\left(-\frac{R_0}{r}\right) - V_m k_{dis} c_{Pt}^{ref} \exp\left(\frac{R_0}{r}\right), \tag{2}$$

with the two kinetic rate constants k_{dis} and k_{rdp}, reflecting the assumption that dissolution proceeds via an oxidized Pt surface, while redeposition occurs on metallic Pt. The reference concentration of dissolved Pt in contact with Pt/C surface is c_{Pt}^{ref}, V_m is the molar volume of Pt. The characteristic radius R_0 depends on the surface tension γ_{Pt} via [56]

$$R_0 = \frac{V_m \gamma_{Pt}}{RT}. \tag{3}$$

The concentration of dissolved Pt $\overline{c_{Pt}}(t)$ is obtained from a mass balance [55],

$$\frac{d\overline{c_{Pt}}(t)}{dt} = -I_v \frac{m_v}{M_{Pt}} \frac{4\pi\rho_{Pt} \int_{0+}^{\infty} r^2 f_N(r,t) \frac{dr}{dt}\, dr}{\frac{4}{3}\pi\rho_{Pt} \int_{0+}^{\infty} r^3 f_N(r,0) dr}, \tag{4}$$

where I_v is the water volume fraction in the catalyst layer, m_v is the Pt mass loading per unit volume, M_{Pt} is the molar mass of Pt, and ρ_{Pt} is the density of Pt. This work does not include the transport of dissolved Pt into the membrane [55] due to the nature of the GDE setup and a limited ability to validate.

Coagulation is described in Eq. (1) with particle creation and extinction terms, J^+ and J^-, respectively, following the Smoluchowski equation. For this, we assume random collisions of the particles and a constant coagulation rate kernel k_{cgl}. Accordingly, creation and extinction terms can be written as [56]

$$J^+ = \frac{1}{2} k_{cgl} \int_{0^+}^{r} \frac{r^2}{\left(r^3 - \tilde{r}^3\right)^{2/3}} f_N\left(\left(r^3 - \tilde{r}^3\right)^{1/3}, t\right) f_N(\tilde{r},t) d\tilde{r}, \tag{5}$$

$$J^- = k_{cgl} \int_{0^+}^{r} f_N(r,t) f_N(\tilde{r},t) d\tilde{r}. \tag{6}$$

Detachment of Pt particles in Eq. (1) is described with a fixed detachment rate k_{det}.

Eq. (1) is solved for $f_N(r,t)$, using Eq. (2)-(6), the free parameters R_0, $k_{dis}, k_{rdp}, k_{cgl}$ and k_{det}, and an initial PRD, $f_N(r,0)$, obtained from the SAXS data. From the resulting $f_N(r,t)$, the temporal evolution of surface area S_N and mass M_N can be obtained as

$$S_N = \frac{\int_{0+}^{\infty} r^2 f_N(r,t) dr}{\int_{0+}^{\infty} r^2 f_N(r,0) dr}, \tag{7}$$

and

$$M_N = \frac{\int_{0+}^{\infty} r^3 f_N(r,t) dr}{\int_{0+}^{\infty} r^3 f_N(r,0) dr}. \tag{8}$$

The physical model was solved with a mass-conserving finite-volume method [57] on a logarithmic radius grid. Parameter fitting was performed in a Bayesian framework detailed in the SI, Table S15. The model was fitted by comparing simulated and measured PRDs on the experimental bin grid and the resulting posterior distribution was used to quantify parameter uncertainty. This approach yields both best-supported parameter values and uncertainty ranges for the corresponding model predictions. It is based on established methods from the literature and was chosen because it is robust to experimental noise, low-signal regions, and detection limits.

3. Results and discussion

3.1. Small Pt/C catalyst – BoL and EoL

We begin the discussion by focusing on the small nanoparticle system, i.e., the Pt/C catalyst with an average particle radius of ~12 Å,

emphasizing the advantages and limitations of the individual *operando* characterization methods applied in this study, i.e., XRD, PDF analysis, and SAXS. We first compare the *operando* data collected at the BoL and the EoL stage of the AST at the center of the catalyst layer, ensuring a consistent basis for comparison. In addition to discussing the advantages and limitations of the individual techniques, we also highlight our analysis strategy for the obtained data.

We first consider the XRD data. XRD provides crucial insights into the crystalline structure of the catalyst particles. Comparing the XRD data of the small Pt nanoparticle system at BoL to those obtained at EoL, see Fig. 2a, it can be seen that the positions of both the BoL and the EoL diffraction peaks agree well with the bulk Pt *fcc* reference. However, while at BoL the Bragg peaks are very broad and on top of a large background signal, the Bragg peaks in the diffraction patterns of the EoL data are sharpened. This is a clear indication of crystallite growth. Applying Rietveld refinements (Figs. S7 and S8, and Tables S3 and S4) of the scale, lattice parameter, and crystallite size to a Pt *fcc* model, we determined an approximate constant lattice parameter which refines to 3.906(5) Å at BoL and EoL, and an increase of the average volume-weighted crystallite radius from around 5 to 11 Å during the AST. We note, however, that for such small nanoparticle sizes, especially at BoL, the XRD method is at its limit due the nanostructure problem. Changes in strain that also contribute to peak broadening were not accounted for in the refinements, as a reliable separation of strain and size was not possible [54]. The quantitative results may thus have a large uncertainty.

PDF is well-suited for characterizing very small nanoparticles (and amorphous and disordered materials) [40–42]. From the PDFs in Fig. 2b, we observe that the most intense peak in the BoL PDF appears at around 2.75 Å, which falls within the expected range of the first Pt–Pt distance in metallic bulk Pt with an *fcc* structure (2.77 Å). Real-space refinement of the scaling, average particle size with an underlying lognormal distribution, and the lattice parameter to a Pt *fcc* model shows a lattice parameter of 3.897(2) Å (Figs. S12 and S13, and Tables S7 and S8). This value is slightly smaller but comparable to the lattice parameter determined from XRD measurements (3.906(5) Å) and that of bulk Pt (3.92316(2) Å) [49].

Upon comparison of the BoL and EoL PDFs, we observe the emergence of peaks at higher r, which correspond to larger Pt–Pt distances in the *fcc* structure within a coherent crystalline domain. This shows a growth of the crystalline domain, as expected from the XRD analysis. The real-space refined average crystallite size with an underlying lognormal distribution of fixed width (Figs. S12 and S13, and Tables S7 and S8) supports this hypothesis, as the crystallite size grows from ca. 6 to 9 Å. At EoL, the refined lattice parameter has increased to 3.913(2) Å. Hence, the PDF analysis at EoL is in good agreement with the XRD results.

With respect to particle size, PDF and XRD analyses provide information on the nanoparticle crystalline domain size, and are not sensitive to, e.g., agglomerates that are not coalesced into a single crystalline phase. This limitation is especially critical in electrocatalysis, where catalytic performance is largely governed by the electrochemically active surface area of agglomerates rather than the properties of individual crystallites. Furthermore, XRD and PDF have limited sensitivity to crystallite size distributions [53]. In *operando* SAXS the signal depends on the size of regions with uniform electron density, representing particle and agglomerate size rather than crystallite size. Conventional SAXS analysis typically assumes a fixed size distribution profile of the particles, such as the Schultz-Zimm, lognormal, or Gaussian distributions [58]. However, as the system degrades, this assumption in the

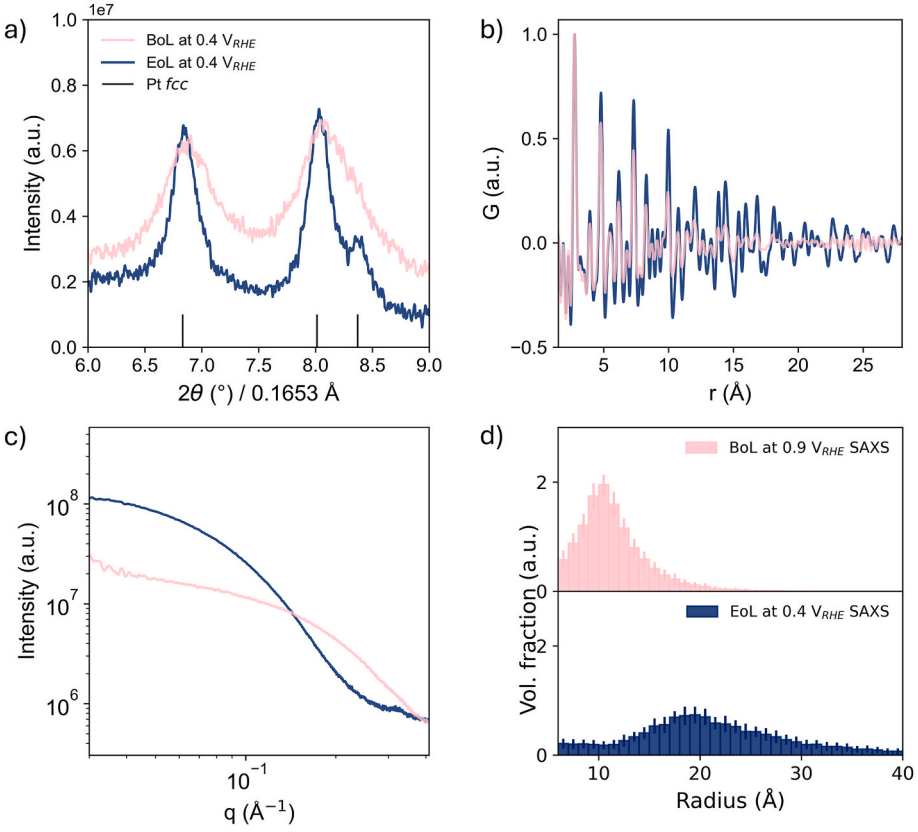

Fig. 2. Data collected at BoL (light pink) and EoL (blue) of the AST measurements. All data were collected at 0.4 V_{RHE} in the center of the Pt/C catalyst layer prepared with the small Pt nanoparticles. a) XRD data, b) PDF data normalised to the highest intensity, to be able to compare the difference in coherent domain size, c) SAXS data, and d) the results from the Monte Carlo analysis of the SAXS data. (For interpretation of the references to color in this figure legend, the reader is referred to the Web version of this article.)

models may become inadequate, failing to accurately capture evolving PRDs. We therefore implemented a Monte Carlo-based analysis of the SAXS data [53]. This approach models the system using spherical scatterers (representing individual nanoparticles) and iteratively adjusts their parameters until the model optimally fits the experimental data based on a predefined figure of merit (χ^2). No prior assumptions about the PRD profile are required. A comparison of the conventional analysis to the Monte Carlo-based approach is shown in Fig. S21 and Table S16, highlighting the need for a non-biased distribution for this. Using the Monte Carlo-based approach, we are able to track dynamic changes in PRD. In Fig. 2c, the SAXS data at BoL and EoL exhibit an apparent shift of the scattering signal to lower *q*, indicating an increase in average particle size. Additionally, the nanoparticles exhibit a high polydispersity based on the absence of distinct scattering features beyond the main feature. The results from the Monte Carlo analysis depicted in Fig. 2d reveal that the average volume-weighted nanoparticle size increased from 12 Å to 22 Å. Hence, from the comparison of the BoL and EoL of the small system with XRD, PDF and SAXS, we can conclude that the crystallite and particle radii are approximately doubled in size between BoL and EoL.

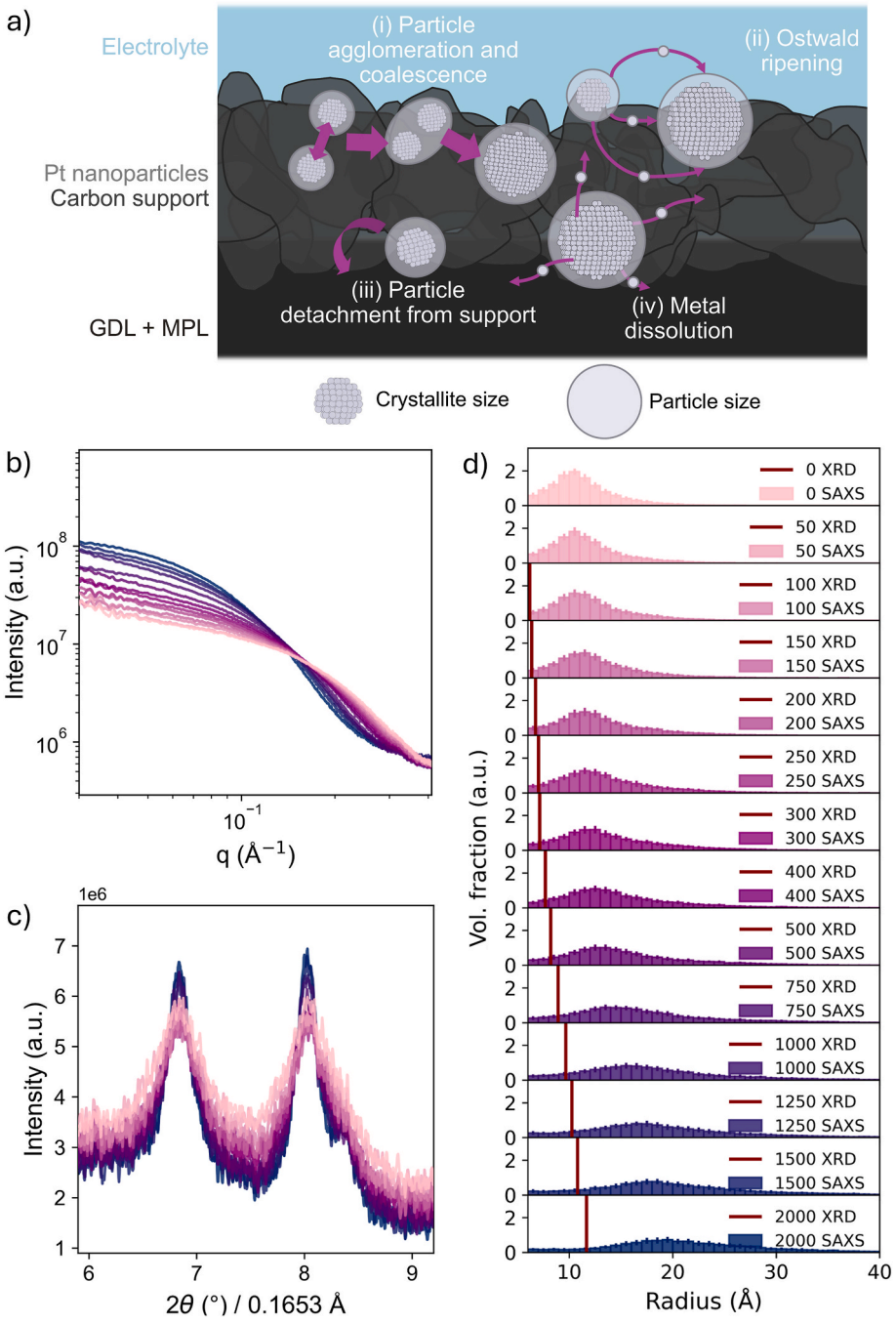

Fig. 3. a) A sketched overview of the degradation mechanisms in the GDE: (i) particle agglomeration followed by coalescence, (ii) Ostwald ripening, (iii) particle detachment, and (iv) particle dissolution. b) SAXS and c) XRD collected for the center layer from a potential hold at 0.9 V_{RHE} after conditioning, i.e., at AST cycle 0, until after the final AST cycle 2000. d) Overview of the results of the Monte Carlo analysis tracking the changes in the particle size radius and the results of the crystallite radius from Rietveld refinements for the XRD of the center catalyst layer. For the first two measurements at AST cycle 0 and 50, the obtained crystallite radii were smaller than the lower minimum of the SAXS analysis and thus not visible.

3.2. Small Pt/C catalyst – during the AST

To continuously monitor these changes and identify the dominant degradation mechanisms, we employed SAXS with Monte Carlo analysis and XRD with Rietveld refinement throughout the entire AST. This multi-scale approach enables us to distinguish between (i) particle agglomeration and coalescence (referred to as coagulation in the modelling), (ii) particle dissolution and redeposition, referred to as Ostwald ripening, (iii) particle detachment, and (iv) particle dissolution without redeposition, as illustrated in Fig. 3a. In particle migration (i), smaller nanoparticles move across the carbon support and agglomerate before they coalesce into larger particles. Agglomeration is expected to appear in the SAXS data as an increased signal corresponding to particles approximately twice their original size, manifested as a tail toward larger radii in the size histograms. In contrast, XRD cannot detected agglomeration; it only reveals coalescence, which is observed as an increase in crystallite size [5]. Ostwald ripening (ii) involves the dissolution of smaller nanoparticles and the redeposition of ionic Pt species onto larger ones. This would result in a concurrent increase in both SAXS- and XRD-derived sizes. Particle detachment from the support (iii) means that catalyst particles are released into the electrolyte, and thus out of the X-ray beam, resulting in a reduced overall scattering intensity and diminished SAXS and XRD signals. Finally, particle dissolution (iv) entails the loss of Pt ions without their subsequent redeposition, reducing both crystallite and particle size as well as the overall scattering signal [5,14,15].

For the small Pt/C system investigated here, the SAXS data presented in Fig. 3b reveal a continuous shift of the scattering profile toward lower q during the AST, indicating particle growth. This aligns with the XRD data presented in Fig. 3c, which shows peak sharpening throughout the AST, indicating continuous crystallite growth. The size histograms derived from the Monte Carlo analysis of the SAXS data combined with the crystallite size from the Rietveld refinements confirm this trend, see Fig. 3d. With increasing AST cycles, a clear shift in the particle radius distribution toward larger radii emerges, most apparent as an extension of the tail of the size distribution toward larger radii from AST cycle 50 onward, ultimately doubling the initial particle radius. Particle growth appears to slow as the AST cycles progress beyond 1500. By comparison, Rietveld refinements of the crystallite size in the XRD data reveal a delayed onset of crystallite growth appearing only after 500 AST cycles, seen Fig. 3c and Fig. S22. This delayed onset of crystallite growth relative to the increase in particle size observed from SAXS is a clear indication of agglomeration and subsequent coalescence [5].

As the number of AST cycles exceeds 1500, the growth trends of crystallite size and particle size begin to align - both slowing down and evolving at a similar rate. Finally, an examination of the volume fraction of the size histograms throughout the entire AST reveals a noticeable decrease in overall volume. Fig. S23 illustrates this phenomenon in terms of particle number density, calculated by dividing the volume fraction by the particle volume, indicating an overall decrease of approximately 70% in particle numbers during the AST.

Taken together, these findings suggest that the very early stages of the AST are dominated by particle migration, leading to agglomeration. In this first degradation phase, small nanoparticles migrate across the carbon support and agglomerate, resulting in an initial rapid increase in particle size (observed by SAXS), while the crystallite size (from XRD) remains relatively unchanged, see (i) in Fig. 3a. Only subsequently does particle coalescence occur, as evidenced by the sharp increase in the growth of the crystallite size after 500 AST cycles. After approximately 1500 AST cycles, a shift in the dominant degradation mechanism occurs. As the larger, agglomerated nanoparticles become less mobile on the carbon support and the overall number of particles decreases, the average distance to the nearest neighbour increases. Consequently, Ostwald ripening becomes more significant, with smaller nanoparticles dissolving in favor of larger ones, (ii) in Fig. 3a. This results in the observed simultaneous increase in both particle and crystallite size; however, the associated growth rate remains significantly lower compared to the rates previously observed during particle agglomeration and coalescence. These observations agree well with findings of Martens et al., who followed the changes of a similar Pt/C system with a particle radius of ca. 15 Å during an AST in a fuel cell using a similar combination of SAXS and XRD. They were able to decouple the degradation mechanism, going from particle agglomeration and eventual coalescence to Ostwald ripening [5].

However, particle agglomeration, coalescence, and Ostwald ripening do not result in a decrease in the overall scattering volume as observed in the histograms from our Monte Carlo analysis. The trends observed in the histograms, as well as in the overall number density, suggest an additional degradation mechanism. Of the change of approximately 70% in number density, only around 50% can be attributed to particle agglomeration. The remaining loss is likely due to particle detachment, a phenomenon proposed from location transmission electron microscopy studies of a similar system [15].

To support these experimentally observed trends and provide a quantitative assessment of the individual degradation mechanisms, a physico-statistical degradation model was fitted to the PRDs obtained from the Monte Carlo analysis. As Fig. 4a shows, the fitted distributions reproduce the experimentally derived PRDs across all AST cycles and over the full relevant particle-size range. Note that deviations in the smallest particle regime below 1 nm are weighted less strongly because this range is particularly susceptible to artefacts in the SAXS-based analysis. Simultaneously, the fit also reproduces the evolution of normalised surface area and captures the normalised Pt mass within experimental uncertainty (see Fig. 4b). Posterior uncertainty is represented by the 25 to 75% and 10 to 90% credible intervals across all plots. Together, these results demonstrate that the model offers a consistent description of the PRDs and integral observables.

Based on this fit, the contributions of the individual degradation mechanisms are deconvoluted with respect to their influence on surface area and Pt mass, as shown in Fig. 4c. The modelling indicates that indeed, Ostwald ripening is the dominant degradation mechanism (see Fig. 4c) as it accounts for nearly the entire surface loss and for most of the Pt mass loss. In contrast, coagulation, which is mass-conserving in the model, does not contribute to mass loss and has only a negligible overall influence. Detachment contributes only a minor fraction of the mass change.

To assess the robustness of this mechanistic interpretation and whether the data can be described with only coagulation and detachment, the fitting was repeated with Ostwald ripening disabled. As shown in Fig. S24, the decrease in surface area is still reproduced reasonably well; however, the evolution of the Pt mass is no longer captured satisfactorily. Furthermore, the agreement with the PRDs is visibly poorer for the most relevant particle radii. The same pattern is reflected by predictive metrics based on the posterior predictions (Table S17). Compared to the full model, the probabilistic prediction error increases significantly for the PRDs, the surface area, and roughly doubles for mass. Consistently, for nearly the same width of the model uncertainty band, 83% of the measured PRD values fall within the central 25-75% range of the full model, compared with only 52% for the “Ostwald ripening-off” variant. From this comparison, we can conclude that the analysis of the change in surface area alone, as for example by using cyclic voltammetry, does not distinguish reliably between the two model variants. However, when Pt mass evolution and PRDs are considered together, the full model describes the data substantially better than the “Ostwald ripening-off” variant. Hence the modelling supports that Ostwald ripening is the dominant mechanism with respect to loss in surface area and Pt mass.

This conclusion should nevertheless be interpreted with caution. The fitted PRDs are reconstructed from SAXS by Monte Carlo analysis and therefore carry uncertainty, particularly for small particles. In addition, the model assumes a homogeneous particle population of spherical nanoparticles and simplified effective kinetics for the individual

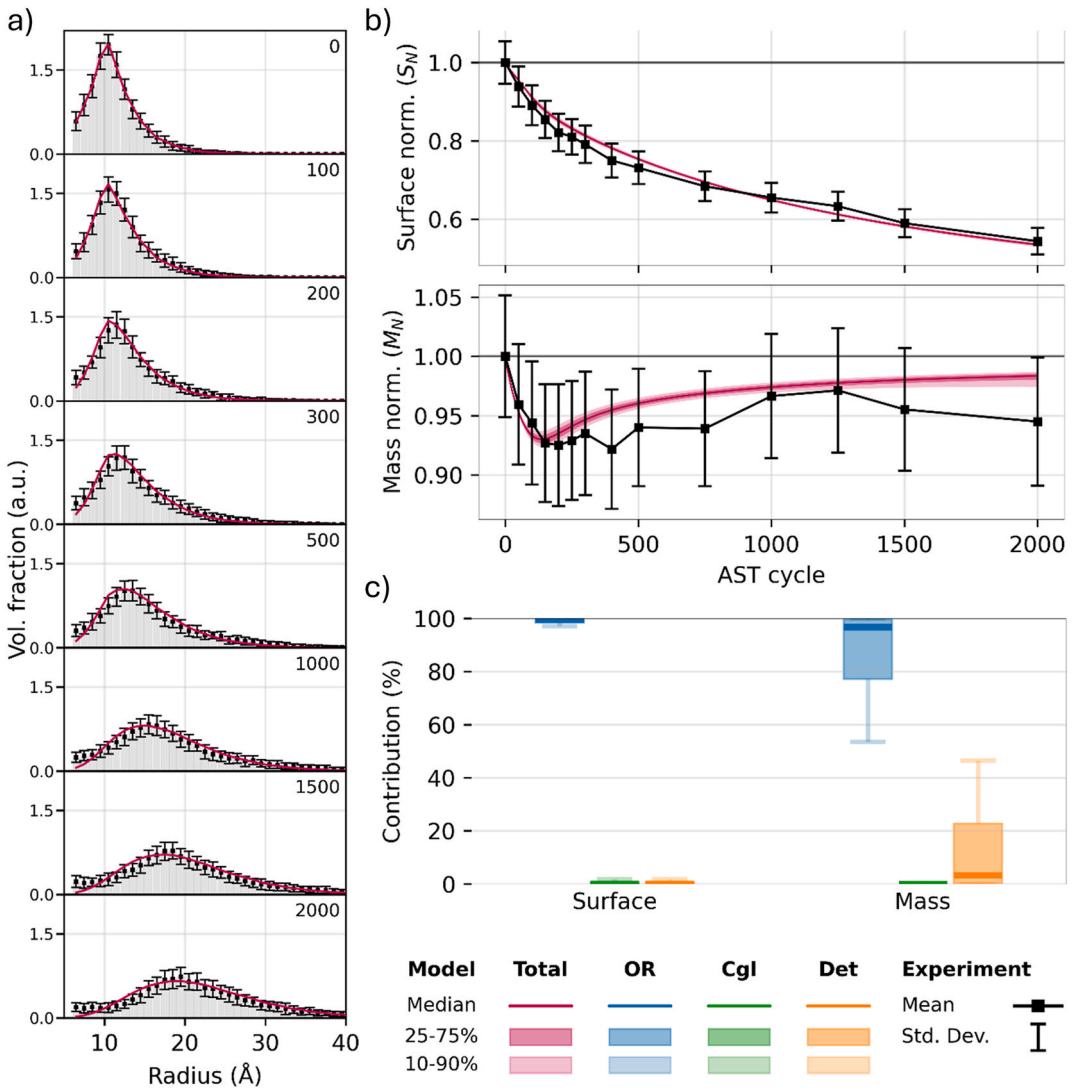

Fig. 4. Full-model fit for the small Pt/C catalyst. a) Comparison of experimentally derived and simulated PRDs at selected AST cycles. b) Evolution of normalised surface area, S_N, and normalised Pt mass, M_N, during the AST. Black symbols show the experimental mean with standard deviation; magenta lines and bands denote the posterior median and the 25-75% and 10-90% credible intervals. c) Deconvoluted model contributions of dissolution and redeposition (Ostwald ripening, OR), coagulation (Cgl), and detachment (Det) to the changes in surface area and mass after 2000 cycles.

degradation mechanisms. The discrepancy with the experiment-based interpretation may therefore reflect both preprocessing uncertainty and model limitations.

3.3. Small Pt/C catalyst – degradation throughout the depth of the catalyst layer

Having successfully decoupled the degradation mechanism at the center of the catalyst layer during the AST, we now turn to investigate depth-dependent trends – specifically, variations as a function of distance from the electrolyte interface. In our previous work by Schröder et al., using a cell with no oxygen flow from the bottom of the GDL, we observed that the depth-dependent degradation of a bimodal Pt/C fuel cell catalyst was most pronounced in the layer closest to the electrolyte [10].

With the more advanced analysis and the new GDE setup operating under high mass transport conditions, we re-investigate depth-dependent changes in the catalyst layer. We first compare the top layer, close to the electrolyte, and then the bottom layer, near the oxygen gas flow from the GDL, see Fig. 5a and b. These layers are positioned 5 µm above and below the center layer. In both the upper and lower layers, the observed general trends are consistent with those in the center layer (Fig. 3c). This is further supported by the trends in the results from the Rietveld refinements and the Monte Carlo analysis, see S25 and S26, respectively. A closer examination of smaller radii in the histograms of Fig. 5a and b, particularly at advanced AST cycles (>500 cycles), reveals a higher volume fraction of smaller particles in the top layer as compared to the bottom layer, as highlighted in the qualitative difference plot in Fig. S27. This difference in the histograms towards the end of the AST suggests a depth-dependent degradation, with the most significant degradation occurring in the bottom layer, i.e., closest to the oxygen gas flow through the GDL. Fig. 5c presents the average particle radius for the three layers throughout the AST supporting a depth-dependent degradation. Hence, our results show the same phenomenon observed in our previous work, however, in opposite layers when operating in a GDE cell.

To further investigate the depth-dependent degradation, we conducted an EoL scan across the catalyst layer and analyzed the particle and crystallite sizes (see Fig. 6 and S28–S31). The EoL SAXS scan reveals a small but significant gradient in particle size with values ranging from 23 Å in the layer furthest from the electrolyte to 22 Å in the layer closest to it. In contrast, the crystalline properties exhibit a different trend. The

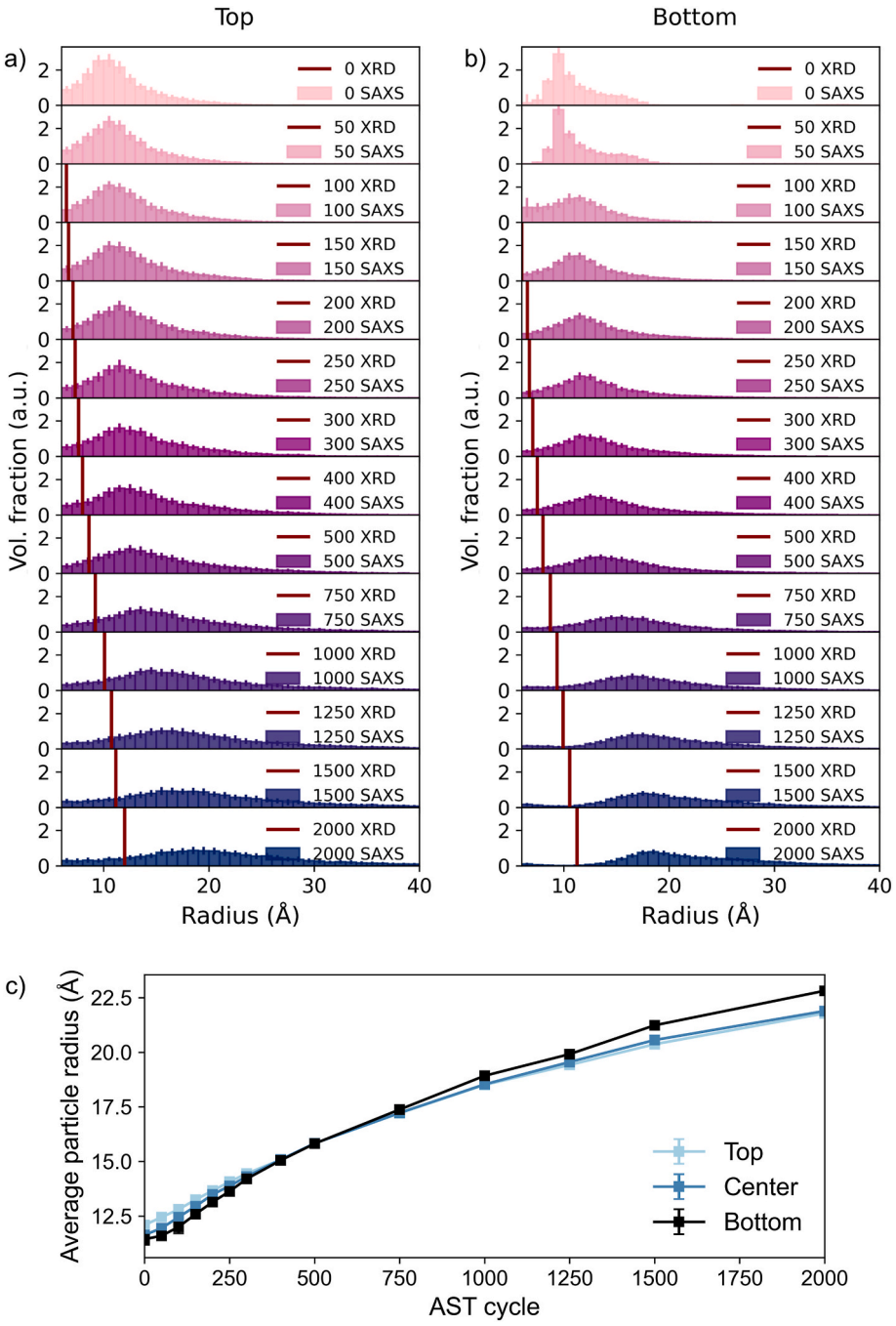

Fig. 5. Overview over the Monte Carlo analysis results tracking the changes in the particle size radius and the results of the crystallite radius from Rietveld refinements for the XRD of the a) top and b) bottom catalyst layer of the small Pt/C catalyst. c) Changes in average particle radius for the three layers throughout the AST.

crystallite sizes obtained from XRD and PDF remain essentially constant across the catalyst layer, with average radii of approximately 11 Å and 9 Å, respectively. The observed particle size gradient compared to the constant crystallite size suggests enhanced agglomeration in the lower layers of the catalyst film, accompanied by a delayed coalescence of crystallites. However, a longer AST would be required to confirm this trend conclusively. To exclude the possibility that the observed gradient arises from the catalyst layer preparation, an additional depth scan was performed at the beginning of the experiment, at open-circuit potential (OCP), immediately after electrolyte addition, and before the conditioning step (Fig. S32–S34). No significant gradient was detected at this stage, confirming that the catalyst layer was initially homogeneous.

As mentioned above, these findings differ from those reported by Schröder et al., who observed pronounced degradation in the layers closest to the liquid electrolyte [10]. In this respect, it is important to note that in the study by Schröder et al., the oxygen mass transport was significantly lower as it occurred as dissolved gas through the electrolyte. In the present work, a direct oxygen mass transport was established through the GDL. Thus, the comparison between these two results suggests more pronounced catalyst degradation in the catalyst layer fraction most exposed to the reactant.

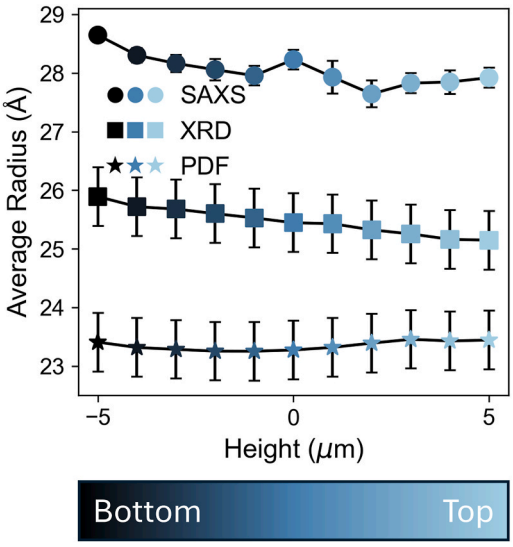

Fig. 6. Overview over the different particle size from SAXS and crystallite size from XRD and PDF throughout the catalyst layer of the small Pt/C catalyst at EoL. The bottom layer is closest to the air and the top to the electrolyte.

3.4. Large Pt/C catalyst

In addition to the small system, we examined a commercial Pt/C catalyst with an average particle radius of about 26 Å to determine whether the trends observed in the small system are size-dependent. We followed the same procedure as for the small system, beginning with an analysis of the XRD, PDF, and SAXS measurements collected at BoL and EoL at 0.4 V_{RHE}.

Comparison of the BoL and EoL XRD data of the center catalyst layer in Fig. 7a reveals only small changes, mainly evident as a loss in intensity over the course of the AST. This indicates stable sizes with only material loss occurring. The stable crystallite and particle sizes are confirmed by Rietveld refinements of the XRD data, which show only a slight crystallite growth from 23 Å to 25 Å, as seen in Fig. 7d–S35, and S36. The PDF data, as seen in Fig. 7b, confirm this observation, and real-space refinements indicate a small increase in average domain from approximately 22 Å to 24 Å. A similar trend is observed in the SAXS data, Fig. 7c, where only a small shift to lower q is detected when comparing BoL and EoL, in contrast to the more pronounced changes seen in the small-particle system. Monte Carlo analysis of the SAXS data indicates particle growth from ca. 27 Å to 28 Å for the center layer, see Fig. 7d–S35 and S37. Some minor artefacts are observed in the histograms at smaller radii, likely due to the low scattering from smaller particles. Fig. 7d also reveals a decrease in overall volume fraction from BoL to EoL, which appears to affect all particle sizes uniformly. This decrease in volume fraction corresponds to a loss of approximately 20% in relative particle number, as shown in Fig. S37.

The trends in particle and crystallite sizes obtained from the Monte Carlo analysis and Rietveld refinement for the center layer, Fig. 7d, indicate that both increase simultaneously. This observation is in contrast to the behavior of the smaller particles discussed above, and the difference may be attributed to the lower mobility of the larger Pt nanoparticles on the carbon support due to their overall larger contact area with the carbon support, making them less prone to migration and agglomeration than smaller Pt particles [14]. It should be noted that these are commercial catalysts for which the synthesis route is not disclosed; thus, differences in degradation mechanisms may additionally arise from the underlying synthesis method. A colloidal synthesis approach would provide a more controlled and homogeneous platform for studying such effects [59]. Interestingly, the extent of particle detachment from the support appears to be similar to that observed in the small particle system. Furthermore, Ostwald ripening alone cannot account for the observed decrease in volume fraction (Fig. 7d and S37).

Next, we turn to the comparative analysis of degradation across the different catalyst layer depths. A comparison between the center layer and the top layer, shown in Fig. 7d and e, respectively, reveals only

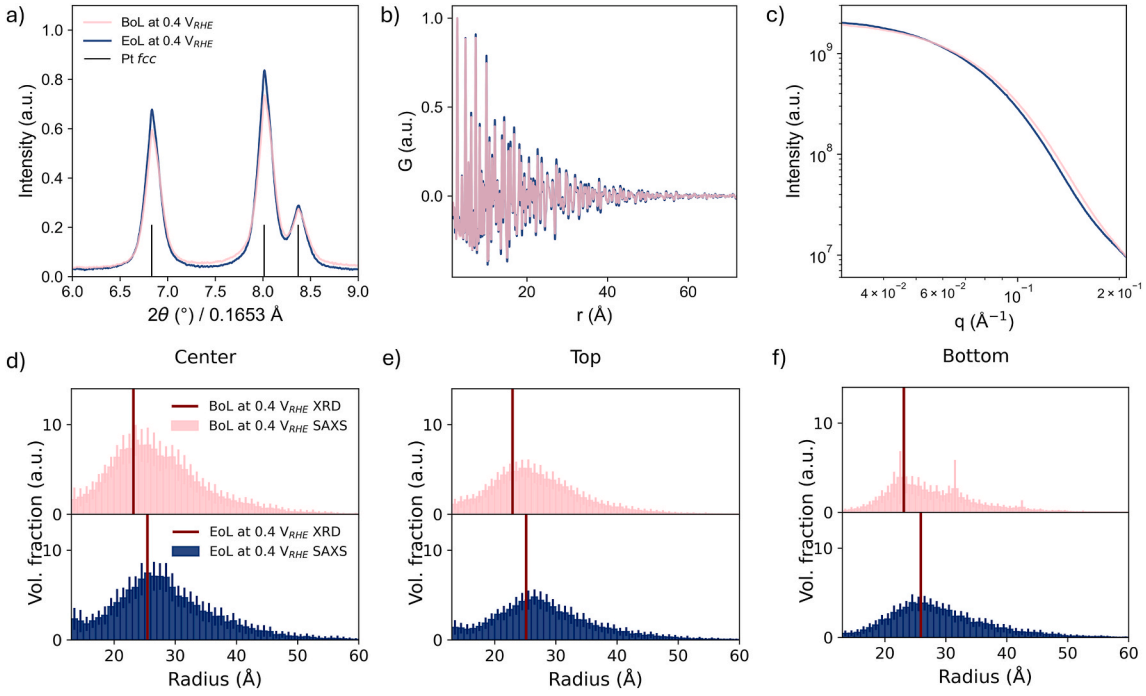

Fig. 7. a) XRD, b) PDF data normalised to the highest intensity, to be able to compare the difference in coherent domain size, and c) SAXS collected at 0.4 V_{RHE} before and after the AST of the large Pt catalyst, measured at the center layer. With the respective overview over the Monte Carlo analysis results tracking the changes in the particle size radius and the results of the crystallite radius from Rietveld refinements for the XRD of the catalyst layer, d) the center layer, e) close to, and f) far from the electrolyte.

minimal differences at both the BoL and EoL. These differences are primarily associated with a reduced overall volume fraction in the top layer, rather than with local deviations at smaller or larger particle radii. The EoL bottom layer, Fig. 7f, exhibits a similar trend, closely matching the top and center layers. An overview of the results is provided in Figs. S37–S39. Notably, in the BoL data, the Monte Carlo analysis performs poorly for the bottom layer. This is likely because only a few particle sizes are sufficient to model the scattering curve, which makes the advanced analysis unstable. A contributing factor may be the complexity of background correction in this region, particularly for layers adjacent to the carbon-rich MPL, where the increased carbon background further complicates the analysis.

These minor differences between the layers, mainly related to the overall volume fraction, are further supported by the qualitative difference plot across the AST (see Fig. S40), which shows only subtle variations within the error margins. This further reinforces the conclusion that there are no significant local deviations in the PRDs across the different depths. A more detailed quantitative analysis of the top layer reveals similar trends in particle growth, with the average particle radius being approximately 1 Å smaller than that of the center layer. Additionally, a ~20% decrease in relative particle number density is observed, consistent with the center layer, see Fig. S39. However, a different trend emerges for the bottom layer. Instead of a decrease, an increase in relative particle number density is observed after around 1000 AST cycles. This may indicate a downward displacement of the catalyst layer, with the center layer, the region of highest Pt scattering intensity, shifting downward and artificially enhancing the apparent Pt signal in the lower layer, an effect that is plausible given the mechanical and chemical complexity of the environment. Consequently, it is not possible to reliably quantify particle detachment for the large-particle system, as was done for the small-particle case. Similarly, the overall extent of depth-dependent particle degradation throughout the AST cannot be determined conclusively.

For a comprehensive understanding of catalyst degradation throughout the entire layer at EoL, we performed a depth-resolved scan, analogous to that conducted for the small Pt system, see Fig. S42–S45. Compared to the pre-AST depth scan, see Fig. S46–S49, the EoL results reveal clear layer-dependent degradation. Fig. 8 presents the final depth profile from the bottom (−5 µm) to the top (+5 µm) layer, incorporating data from PDF, XRD, and SAXS analyses. The SAXS analysis shows a negative gradient in particle size of approximately 1 Å from the bottom to the top layer, with further details provided in Fig. S44. A similar gradient in crystallite domain size - also around 1 Å - is observed in the XRD data, see Fig. S43. In contrast, the PDF data exhibits a more constant trend across the layers, see Fig. S44.

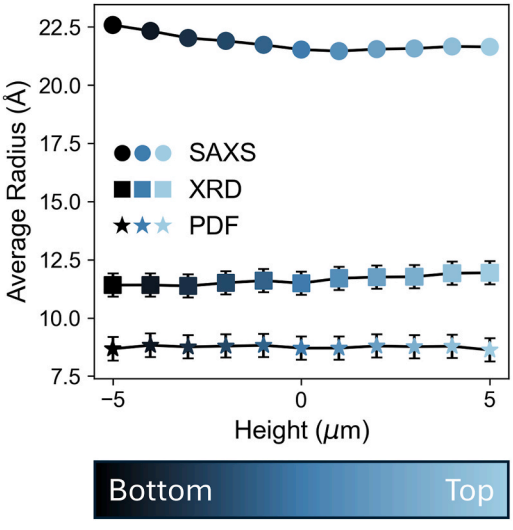

Fig. 8. Overview over the different particle size from SAXS and crystallite size from XRD and PDF throughout the catalyst layer of the large system at the EoL. The bottom is closest to the Carbon and the top to the electrolyte.

Overall, the observed downward trend in both particle and crystallite sizes in the large-particle system partially mirrors the behavior of the small-particle system. However, in the large-particle, only the particle size exhibited a depth-dependent gradient, while crystallite size remained unchanged. This distinction likely reflects a fundamental difference in degradation mechanisms: in the large system, no initial nanoparticle migration across the carbon support is observed before the increase in crystallite size. Nonetheless, the results confirm that the degradation in the large-particle system is also depth-dependent, reinforcing our earlier conclusion that catalyst degradation occurs preferentially in regions most exposed to the reactants, where reaction rates are highest.

Following the same approach as for the small-particle catalyst, we used the physico-statistical model to provide a quantitative assessment of the individual degradation mechanisms. The full model was fitted to the PRDs obtained from the Monte Carlo analysis and, consistently, to the normalised surface area and normalised Pt mass. Since the pre-processed data shows an unexpected loss of particles compared to the bottom layer toward the end of the experiment (see Fig. S37), the fitting was restricted to the first 1000 AST cycles to avoid capturing potential experimental artefacts. As shown in Fig. 9a and b, the model reproduces the PRDs, as well as the decreases in surface area and mass within experimental uncertainty. However, the good agreement of the model should not be overinterpreted mechanistically. Because the total degradation is small, the data provide only weak constraints on the relative importance of the individual mechanisms. Accordingly, the mechanistic deconvolution shows broad posterior ranges, i.e. large uncertainties, for the contributions of the different mechanisms (see Fig. 9c). Although the posterior medians tend to favor Ostwald ripening, a robust quantitative separation of the mechanisms from the model fit is not possible for the large Pt/C catalyst.

4. Conclusion

The combination of *operando* SAXS, XRD, and PDF, along with Monte Carlo analysis, Rietveld, and real-space refinements, and a model-based analysis, provides unprecedented details into the dominant degradation mechanisms of commercial Pt/C catalyst systems in GDEs, as summarized in Fig. 10.

For catalysts composed of small Pt nanoparticles (here ~12 Å average radius), we observe a progressive transition in degradation mechanisms: beginning with particle migration and agglomeration during the early stages of the AST, followed by particle coalescence and ultimately Ostwald ripening. In addition, we detect signs of particle detachment. The model-based analysis supports Ostwald ripening to be the overall dominant mechanism with respect to surface area and Pt mass loss. Depth-resolved analysis shows that catalyst degradation is depth-dependent, with the most pronounced degradation occurring in the layers closest to the oxygen gas flow. Comparison with previous results suggests that experimental setups lacking reactant mass transport through a gas diffusion layer may underestimate the full extent of catalyst degradation across the entire catalyst layer.

For larger Pt nanoparticles (here ~26 Å average radius), no initial particle agglomeration is observed. Instead, Ostwald ripening is the dominant degradation pathway from the onset of the AST. While the trend in depth-dependent degradation mirrors that of the small-particle system, the degradation appears more uniformly governed by ripening. As with the smaller system, particle detachment is observed, potentially having a more pronounced effect on the overall surface area loss. The model-based analysis for the larger Pt nanoparticles has a high uncertainty due to the relatively small overall degradation. It suggests the contribution of various degradation mechanisms, giving Ostwald ripening only a slightly higher probability than detachment.

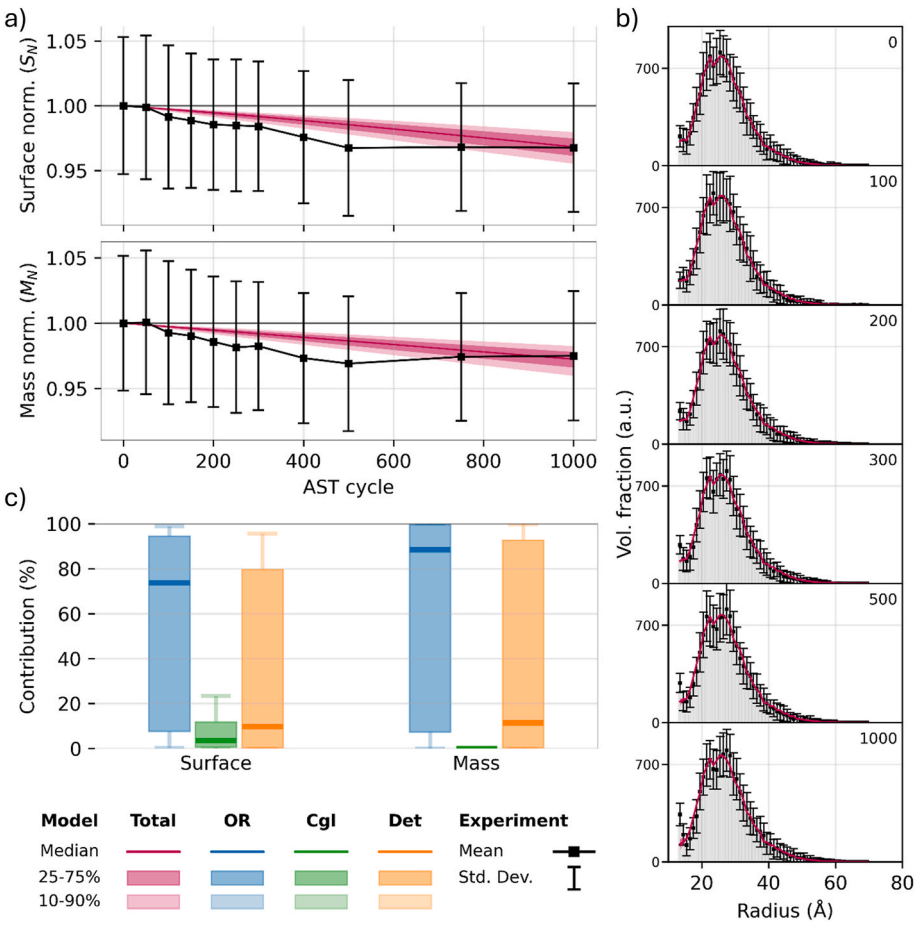

Fig. 9. Full-model fit for the large Pt/C catalyst, a) Evolution of normalised surface area, and normalised Pt mass, during the AST. Black symbols show the experimental mean with standard deviation; magenta lines and bands denote the posterior median and the 25-75% and 10-90% credible intervals. b) Comparison of experimentally derived and fitted particle radius distributions (PRDs) at selected AST cycles. c) Deconvoluted model contributions of dissolution and redeposition (Ostwald ripening, OR), coagulation (Cgl), and detachment (Det) to the changes in surface area and mass after 1000 cycles.

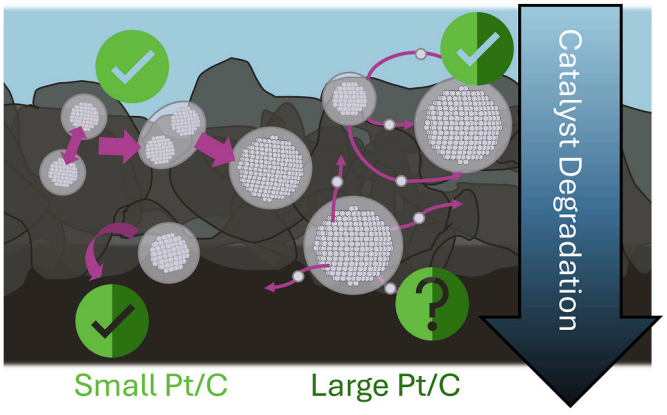

Fig. 10. Qualitative sketch of the different degradation mechanisms present in the small and large Pt/C catalysts, as well as the degradation extent throughout the whole layer indicated by the arrow.

Together, these findings offer a nuanced understanding of the interplay between particle size, degradation mechanism, and catalyst layer depth -highlighting the importance of studying catalyst systems under realistic, high-mass-transport conditions. Based on these findings, we propose a gradient catalyst architecture, with a layer of larger Pt nanoparticles positioned closer to the gas flow and a layer of smaller Pt nanoparticles located closer to the electrolyte/membrane interface.

Use of AI in writing process

During the preparation of this work, the authors used ChatGPT-4o for the correction of language and grammar. No complete sections were written nor was any reference added with the help of AI tools. The authors reviewed and edited the output as needed and take full responsibility for the content of the published article.

CRediT authorship contribution statement

Stefanie Punke: Conceptualization, Data curation, Formal analysis, Investigation, Visualization, Writing – original draft, Writing – review & editing. **Jannik Heitz:** Data curation, Formal analysis, Visualization, Writing – review & editing. **Rebecca K. Pittkowski:** Conceptualization, Investigation, Supervision, Writing – original draft, Writing – review & editing. **Jens Edelvang-Pejrup:** Investigation, Writing – review & editing. **Aline Bornet:** Investigation, Writing – review & editing. **Jakub Drnec:** Investigation, Resources, Writing – review & editing. **Jacob J.K. Kirkensgaard:** Supervision, Validation, Writing – review & editing. **Thomas Kadyk:** Supervision, Validation, Writing – review & editing. **Kirsten M. Ø. Jensen:** Conceptualization, Funding acquisition, Project administration, Supervision, Writing – original draft, Writing – review & editing. **Matthias Arenz:** Conceptualization, Funding acquisition, Investigation, Project administration, Supervision, Writing – original draft, Writing – review & editing.

Declaration of competing interest

The authors declare that they have no known competing financial interests or personal relationships that could have appeared to influence the work reported in this paper.

Acknowledgements

The authors acknowledge the support from the Danish National Research Foundation Center for High-Entropy Alloy Catalysis (CHEAC) DNRF-149, Denmark. MA and RP acknowledge funding from the Swiss National Science Foundation via grant 10001494, Switzerland. The Danish Research Council is acknowledged for covering travel expenses concerning the synchrotron experiments (DanScatt), Denmark. The European Synchrotron Research Facility (ESRF) is gratefully acknowledged for the provision of beamtime at beamline ID31 through proposal CH 6560, DOI: 10.15151/ESRF-ES-1083195956.

Appendix A. Supplementary data

Supplementary data to this article can be found online at https://doi.org/10.1016/j.ijhydene.2026.156827.

References

[1] Pollet BG, Kocha SS, Staffell I. Current status of automotive fuel cells for sustainable transport. Curr Opin Electrochem 2019;16:90–5. https://doi.org/10.1016/j.coelec.2019.04.021.
[2] Banham D, Ye S. Current status and future development of catalyst materials and catalyst layers for proton exchange membrane fuel cells: an industrial perspective. ACS Energy Lett 2017;2:629–38. https://doi.org/10.1021/acsenergylett.6b00644.
[3] Cullen DA, Neyerlin KC, Ahluwalia RK, Mukundan R, More KL, Borup RL, Weber AZ, Myers DJ, Kusoglu A. New roads and challenges for fuel cells in heavy-duty transportation. Nat Energy 2021;6:462–74. https://doi.org/10.1038/s41560-021-00775-z.
[4] Kodama K, Nagai T, Kuwaki A, Jinnouchi R, Morimoto Y. Challenges in applying highly active Pt-based nanostructured catalysts for oxygen reduction reactions to fuel cell vehicles. Nat Nanotechnol 2021;16:140–7. https://doi.org/10.1038/s41565-020-00824-w.
[5] Martens I, Chattot R, Drnec J. Decoupling catalyst aggregation, ripening, and coalescence processes inside operating fuel cells. J Power Sources 2022;521:230851. https://doi.org/10.1016/j.jpowsour.2021.230851.
[6] Meier JC, Galeano C, Katsounaros I, Topalov AA, Kostka A, Schüth F, Mayrhofer KJJ. Degradation mechanisms of Pt/C fuel cell catalysts under simulated start–stop conditions. ACS Catal 2012;2:832–43. https://doi.org/10.1021/cs300024h.
[7] Cherevko S, Kulyk N, Mayrhofer KJJ. Durability of platinum-based fuel cell electrocatalysts: dissolution of bulk and nanoscale platinum. Nano Energy 2016;29:275–98. https://doi.org/10.1016/j.nanoen.2016.03.005.
[8] Redmond PL, Hallock AJ, Brus LE. Electrochemical ostwald ripening of colloidal Ag particles on conductive substrates. Nano Lett 2005;5:131–5. https://doi.org/10.1021/nl048204r.
[9] Redmond EL, Setzler BP, Juhas P, Billinge SJL, Fuller TF. In-Situ monitoring of particle growth at PEMFC cathode under accelerated cycling conditions. Electrochem Solid State Lett 2012;15:72–4. https://doi.org/10.1149/2.004206esl.
[10] Schroder J, Pittkowski RK, Martens I, Chattot R, Drnec J, Quinson J, Kirkensgaard JJK, Arenz M. Tracking the catalyst layer depth-dependent electrochemical degradation of a bimodal Pt/C fuel cell catalyst: a combined operando Small- and wide-angle X-ray scattering study. ACS Catal 2022;12:2077–85. https://doi.org/10.1021/acscatal.1c04365.
[11] Chattot R, Mirolo M, Martens I, Kumar K, Martin V, Gasmi A, Dubau L, Maillard F, Castanheira L, Drnec J. Beware of cyclic voltammetry! measurement artefact in accelerated stress test of fuel cell cathode revealed by operando X-ray diffraction. J Power Sources 2023;555:232345. https://doi.org/10.1016/j.jpowsour.2022.232345.
[12] Ferreira PJ, la O GJ, Shao-Horn Y, Morgan D, Makharia R, Kocha S, Gasteiger HA. Instability of Pt/C electrocatalysts in proton exchange membrane fuel cells - a mechanistic investigation. J Electrochem Soc 2005;152:A2256–71. https://doi.org/10.1149/1.2050347.
[13] Borup R, Meyers J, Pivovar B, Kim YS, Mukundan R, Garland N, Myers D, Wilson M, Garzon F, Wood D, Zelenay P, More K, Stroh K, Zawodzinski T, Boncella J, McGrath JE, Inaba M, Miyatake K, Hori M, Ota K, Ogumi Z, Miyata S, Nishikata A, Siroma Z, Uchimoto Y, Yasuda K, Kimijima K-i, Iwashita N. Scientific aspects of polymer electrolyte fuel cell durability and degradation. Chem Rev 2007;107:3904–51. https://doi.org/10.1021/cr050182l.
[14] Kregar A, Kravos A, Katrašnik T. Methodology for evaluation of contributions of ostwald ripening and particle agglomeration to growth of catalyst particles in PEM fuel cells. Fuel Cells 2020;20:487–98. https://doi.org/10.1002/fuce.201900208.
[15] Mayrhofer KJJ, Meier JC, Ashton SJ, Wiberg GKH, Kraus F, Hanzlik M, Arenz M. Fuel cell catalyst degradation on the nanoscale. Electrochem Commun 2008;10:1144–7. https://doi.org/10.1016/j.elecom.2008.05.032.
[16] Chattot R, Roiron C, Kumar K, Martin V, Campos Roldan CA, Mirolo M, Martens I, Castanheira L, Viola A, Bacabe R, Cavaliere S, Blanchard P-Y, Dubau L, Maillard F, Drnec J. Break-In bad: on the conditioning of fuel cell nanoalloy catalysts. ACS Catal 2022;12:15675–85. https://doi.org/10.1021/acscatal.2c04495.
[17] Granqvist CG, Buhrman RA. Size distributions for supported metal catalysts: coalescence growth versus ostwald ripening. J Catal 1976;42:477–9. https://doi.org/10.1016/0021-9517(76)90125-1.
[18] Ohma A, Shinohara K, Iiyama A, Yoshida T, Daimaru A. Membrane and catalyst performance targets for automotive fuel cells by FCCJ membrane, catalyst. MEA WG, ECS Trans 2011;41:775. https://doi.org/10.1149/1.3635611.
[19] Schroder J, Pittkowski RK, Du J, Kirkensgaard JJK, Arenz M. Investigating the particle growth in bimodal Pt/C catalysts by In-Situ small-angle X-ray scattering: challenges in the evaluation of stress test protocol-dependent degradation mechanisms. J Electrochem Soc 2022;169:7. https://doi.org/10.1149/1945-7111/ac99a5.
[20] Alinejad S, Inaba M, Schröder J, Du J, Quinson J, Zana A, Arenz M. Testing fuel cell catalysts under more realistic reaction conditions: accelerated stress tests in a gas diffusion electrode setup. JPhys Energy 2020;2:024003. https://doi.org/10.1088/2515-7655/ab67e2.
[21] Pizzutilo E, Geiger S, Grote JP, Mingers A, Mayrhofer KJJ, Arenz M, Cherevko S. On the need of improved accelerated degradation protocols (ADPs): examination of platinum dissolution and carbon corrosion in half-cell tests. J Electrochem Soc 2016;163:F1510. https://doi.org/10.1149/2.0731614jes.
[22] Hartl K, Hanzlik M, Arenz M. IL-TEM investigations on the degradation mechanism of Pt/C electrocatalysts with different carbon supports. Energy Environ Sci 2011;4:234–8. https://doi.org/10.1039/C0EE00248H.
[23] Hodnik N, Zorko M, Bele M, Hočevar S, Gaberšček M. Identical location scanning electron microscopy: a case study of electrochemical degradation of PtNi nanoparticles using a new nondestructive method. J Phys Chem C 2012;116:21326–33. https://doi.org/10.1021/jp303831c.
[24] Zana A, Speder J, Roefzaad M, Altmann L, Bäumer M, Arenz M. Probing degradation by IL-TEM: the influence of stress test conditions on the degradation mechanism. J Electrochem Soc 2013;160:F608. https://doi.org/10.1149/2.078306jes.
[25] Arenz M, Zana A. Fuel cell catalyst degradation: identical location electron microscopy and related methods. Nano Energy 2016;29:299–313. https://doi.org/10.1016/j.nanoen.2016.04.027.
[26] Schonvogel D, Hülstede J, Wagner P, Kruusenberg I, Tammeveski K, Dyck A, Agert C, Wark M. Stability of Pt nanoparticles on alternative carbon supports for oxygen reduction reaction. J Electrochem Soc 2017;164:F995. https://doi.org/10.1149/2.1611709jes.
[27] Souza NE, Bott-Neto JL, Rocha TA, da Silva GC, Teixeira-Neto E, Gonzalez ER, Ticianelli EA. Support modification in Pt/C electrocatalysts for durability increase: a degradation study assisted by identical location transmission electron microscopy. Electrochim Acta 2018;265:523–31. https://doi.org/10.1016/j.electacta.2018.01.180.
[28] Lafforgue C, Maillard F, Martin V, Dubau L, Chatenet M. Degradation of carbon-supported platinum-group-metal electrocatalysts in alkaline media studied by in situ fourier transform infrared spectroscopy and identical-location transmission electron microscopy. ACS Catal 2019;9:5613–22. https://doi.org/10.1021/acscatal.9b00439.
[29] Yu H, Zachman M, Myers D, Mukundan R, Zhang H, Zelenay P, Neyerlin K, Cullen D. Elucidating fuel cell catalyst degradation mechanisms by identical-location transmission electron microscopy. Microsc Microanal 2021;27:974–6. https://doi.org/10.1017/s1431927621003706.
[30] Schröder J, Quinson J, Mathiesen JK, Kirkensgaard JJK, Alinejad S, Mints VA, Jensen KM, Arenz M. A new approach to probe the degradation of fuel cell catalysts under realistic conditions: combining tests in a gas diffusion electrode setup with small angle X-ray scattering. J Electrochem Soc 2020;167:134515. https://doi.org/10.1149/1945-7111/abbdd2.
[31] Alinejad S, Quinson J, Schroder J, Kirkensgaard JJK, Arenz M. Carbon-supported platinum electrocatalysts probed in a gas diffusion setup with alkaline environment: how particle size and mesoscopic environment influence the degradation mechanism. ACS Catal 2020;10:13040–9. https://doi.org/10.1021/acscatal.0c03184.
[32] Scott SB, Hogg TV, Landers AT, Maagaard T, Bertheussen E, Lin JC, Davis RC, Beeman JW, Higgins D, Drisdell WS, Hahn C, Mehta A, Seger B, Jaramillo TF, Chorkendorff I. Absence of oxidized phases in Cu under CO reduction conditions. ACS Energy Lett 2019;4:803–4. https://doi.org/10.1021/acsenergylett.9b00172.
[33] Martens I, Chattot R, Rasola M, Blanco MV, Honkimäki V, Bizzotto D, Wilkinson DP, Drnec J. Probing the dynamics of platinum surface oxides in fuel cell catalyst layers using in situ X-ray diffraction. ACS Appl Energy Mater 2019;2:7772–80. https://doi.org/10.1021/acsaem.9b00982.
[34] Martens I, Chattot R, Wiegmann T, Fuchs T, Magnussen OM, Dubau L, Maillard F, Drnec J. Towards comprehensive understanding of proton-exchange membrane fuel cells using high energy x-rays. JPhys Energy 2021;3:031003. https://doi.org/10.1088/2515-7655/abf43d.
[35] Magnussen OM, Drnec J, Qiu C, Martens I, Huang JJ, Chattot R, Singer A. In situ and operando X-ray scattering methods in electrochemistry and electrocatalysis. Chem Rev 2024;124:629–721. https://doi.org/10.1021/acs.chemrev.3c00331.
[36] Bogar M, Yakovlev Y, Pollastri S, Biagi R, Amenitsch H, Taccani R, Matolínová I. Capabilities of a novel electrochemical cell for operando XAS and SAXS

investigations for PEM fuel cells and water electrolysers, 615; 2024, 235070. https://doi.org/10.1016/j.jpowsour.2024.235070.
[37] Povia M, Herranz J, Binninger T, Nachtegaal M, Diaz A, Kohlbrecher J, Abbott DF, Kim B-J, Schmidt TJ. Combining SAXS and XAS to study the operando degradation of carbon-supported Pt-Nanoparticle. Fuel Cell Catalysts 2018;8:7000–15. https://doi.org/10.1021/acscatal.8b01321.
[38] Wiberg GKH, Pittkowski RK, Punke S, Aalling-Frederiksen O, Schlegel N, Jensen K, Arenz M. Corrigendum: design and application of a gas diffusion electrode (GDE) cell for operando and in situ studies. Chimia 2024;78:682. https://doi.org/10.2533/chimia.2024.682.
[39] Riasse R, Lafforgue C, Vandenberghe F, Micoud F, Morin A, Arenz M, Durst J, Chatenet M. Benchmarking proton exchange membrane fuel cell cathode catalyst at high current density: a comparison between the rotating disk electrode, the gas diffusion electrode and differential cell. J Power Sources 2023;556:232491. https://doi.org/10.1016/j.jpowsour.2022.232491.
[40] Pittkowski RK, Punke S, Anker AS, Bornet A, Magnard NPL, Schlegel N, Graversen LG, Quinson J, Dworzak A, Oezaslan M, Kirkensgaard JJK, Mirolo M, Drnec J, Arenz M, Jensen KMØ. Monitoring the structural changes in iridium nanoparticles during oxygen evolution electrocatalysis with operando X-ray total scattering. J Am Chem Soc 2024;146:27517–27. https://doi.org/10.1021/jacs.4c08149.
[41] Aalling-Frederiksen O, Schlegel N, Punke S, Anker AS, Wiberg GKH, Wang B, Edelvang-Pejrup J, Holde FB, Salinas-Quezada MP, Magnard NPL, Graversen LG, Arenz M, Pittkowski RK, Jensen KMØ. Structural changes of NiFe layered double hydroxides during the oxygen evolution reaction: a diffraction and total scattering operando study. Small 2025;21:2411211. https://doi.org/10.1002/smll.202411211.
[42] Christiansen TL, Cooper SR, Jensen KMO. There's no place like real-space: elucidating size-dependent atomic structure of nanomaterials using pair distribution function analysis. Nanoscale Adv 2020;2:2234–54. https://doi.org/10.1039/d0na00120a.
[43] Martens I, Vamvakeros A, Chattot R, Blanco MV, Rasola M, Pusa J, Jacques SDM, Bizzotto D, Wilkinson DP, Ruffmann B, Heidemann S, Honkimäki V, Drnec J. X-ray transparent proton-exchange membrane fuel cell design for in situ wide and small angle scattering tomography. J Power Sources 2019;437:226906. https://doi.org/10.1016/j.jpowsour.2019.226906.
[44] Mirolo M, Isern H, Rusello F, Vinci V, Deissler NH, Stando M, Punke S, Ruellou J, Honkimaki V, Drnec J. ID31 beamline of ESRF: the ultimate tool for operando characterization of electrocatalytic systems. Synchrotron Radiat News 2026:1–8. https://doi.org/10.1080/08940886.2026.2627161.
[45] Urchaga P, Kadyk T, Rinaldo SG, Pistono AO, Hu J, Lee W, Richards C, Eikerling MH, Rice CA. Catalyst degradation in fuel cell electrodes: accelerated stress tests and model-based analysis. Electrochim Acta 2015;176:1500–10. https://doi.org/10.1016/j.electacta.2015.03.152.
[46] Yarlagadda V, McKinney SE, Keary CL, Thompson L, Zulevi B, Kongkanand A. Preparation of PEMFC electrodes from milligram-amounts of catalyst powder. J Electrochem Soc 2017;164:F845. https://doi.org/10.1149/2.1461707jes.
[47] Ashiotis G, Deschildre A, Nawaz Z, Wright JP, Karkoulis D, Picca FE, Kieffer J. The fast azimuthal integration Python library: pyFAI. J Appl Crystallogr 2015;48:510–9. https://doi.org/10.1107/S1600576715004306.
[48] Coelho A. TOPAS and TOPAS-Academic: an optimization program integrating computer algebra and crystallographic objects written in C++. J Appl Crystallogr 2018;51:210–8. https://doi.org/10.1107/S1600576718000183.
[49] Hong KH, McNally GM, Coduri M, Attfield JP. Synthesis, crystal structure, and magnetic properties of MnFe3O5. Z Anorg Allg Chem 2016;642:1355–8. https://doi.org/10.1002/zaac.201600365.
[50] Juhas P, Davis T, Farrow CL, Billinge SJL. PDFgetX3: a rapid and highly automatable program for processing powder diffraction data into total scattering pair distribution functions. J Appl Crystallogr 2013;46:560–6. https://doi.org/10.1107/S0021889813005190.
[51] Gamez-Mendoza L, Terban MW, Billinge SJL, Martinez-Inesta M. Modelling and validation of particle size distributions of supported nanoparticles using the pair distribution function technique. J Appl Crystallogr 2017;50:741–8. https://doi.org/10.1107/s1600576717003715.
[52] Juhás P, Farrow CL, Yang X, Knox KR, Billinge SJ. Complex modeling: a strategy and software program for combining multiple information sources to solve ill posed structure and nanostructure inverse problems. Acta Crystallogr A 2015;71:562–8. https://doi.org/10.1107/s2053273315014473.
[53] Bressler I, Pauw BR, Thunemann AF. McSAS: software for the retrieval of model parameter distributions from scattering patterns. J Appl Crystallogr 2015;48:962–9. https://doi.org/10.1107/S1600576715007347.
[54] Ingham B. X-ray scattering characterisation of nanoparticles. Crystallogr Rev 2015;21:229–303. https://doi.org/10.1080/0889311X.2015.1024114.
[55] Baroody HA, Stolar DB, Eikerling MH. Modelling-based data treatment and analytics of catalyst degradation in polymer electrolyte fuel cells. Electrochim Acta 2018;283:1006–16. https://doi.org/10.1016/j.electacta.2018.06.108.
[56] Rinaldo SG, Lee W, Stumper J, Eikerling M. Nonmonotonic dynamics in lifshitz-slyozov-wagner theory: ostwald ripening in nanoparticle catalysts. Phys Rev E 2012;86:041601. https://doi.org/10.1103/PhysRevE.86.041601.
[57] O'Sullivan D, Rigopoulos S. A conservative finite volume method for the population balance equation with aggregation, fragmentation, nucleation and growth. Chem Eng Sci 2022;263:117925. https://doi.org/10.1016/j.ces.2022.117925.
[58] Li T, Senesi AJ, Lee B. Small angle X-ray scattering for nanoparticle research. Chem Rev 2016;116:11128–80. https://doi.org/10.1021/acs.chemrev.5b00690.
[59] Quinson J, Kunz S, Arenz M. Surfactant-free colloidal syntheses of precious metal nanoparticles for improved catalysts. ACS Catal 2023;13:4903–37. https://doi.org/10.1021/acscatal.2c05998.